Title: Carbamazepine degradation using a N-doped TiO_2 coated photocatalytic membrane reactor: influence of physical parameters

Author: Inna Horovitz Dror Avisar Mark A. Baker Rossana Grilli Luca Lozzi Daniela Di Camillo Hadas Mamane

PII: S0304-3894(16)30097-8
DOI: http://dx.doi.org/doi:10.1016/j.jhazmat.2016.02.008
Reference: HAZMAT 17441

To appear in: *Journal of Hazardous Materials*

Received date: 13-11-2015
Revised date: 17-1-2016
Accepted date: 2-2-2016

Please cite this article as: Inna Horovitz, Dror Avisar, Mark A.Baker, Rossana Grilli, Luca Lozzi, Daniela Di Camillo, Hadas Mamane, Carbamazepine degradation using a N-doped TiO2 coated photocatalytic membrane reactor: influence of physical parameters, Journal of Hazardous Materials http://dx.doi.org/10.1016/j.jhazmat.2016.02.008

Carbamazepine degradation using a N-doped TiO_2 coated photocatalytic membrane reactor: influence of physical parameters

Inna Horovitz[a,b], Dror Avisar[b], Mark A. Baker[c], Rossana Grilli[c], Luca Lozzi[d], Daniela Di Camillo[d], Hadas Mamane[a,*]

[a]*School of Mechanical Engineering, Faculty of Engineering, Tel Aviv University, Tel Aviv 69978, Israel*

[b]*The Hydro-Chemistry Laboratory, Faculty of Geography and the Environment, Tel Aviv University, Tel Aviv 69978, Israel*

[c]*The Surface Analysis Laboratory, Faculty of Engineering and Physical Sciences, University of Surrey, Guildford, Surrey, GU2 7XH, UK*

[d]*Department of Physical and Chemical Sciences, University of L'Aquila, Via Vetoio, I-67100 L'Aquila, Italy*

* Corresponding author: Tel.: +972 3 6408129; fax: +972 3 6407334.

E-mail address: hadasmg@post.tau.ac.il (H. Mamane).

Graphical abstract

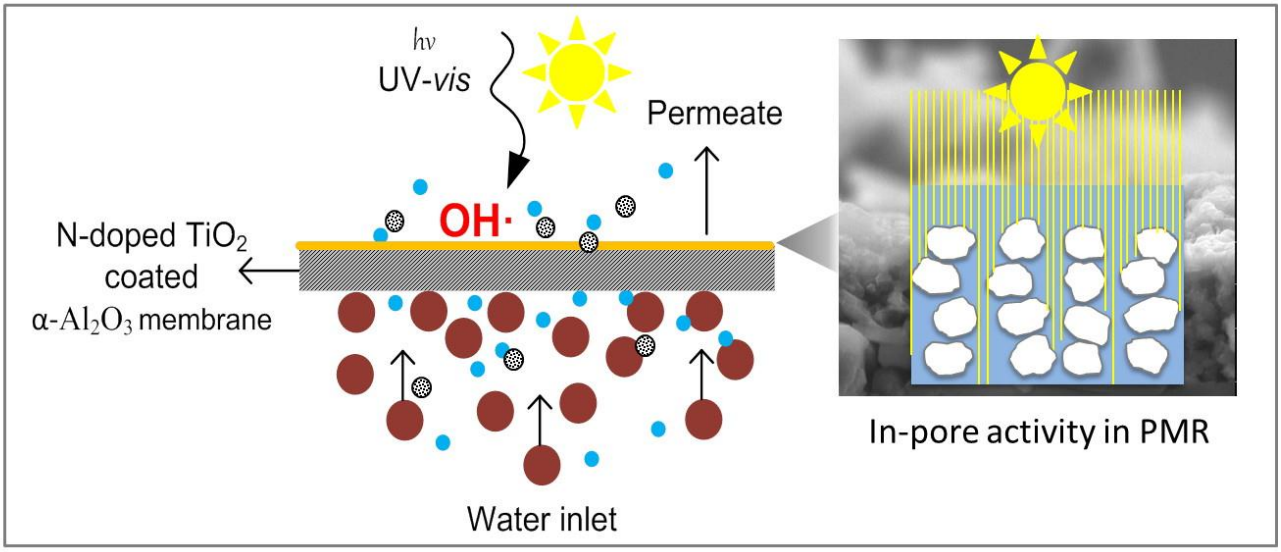

Highlights

- UV-*vis* N-doped TiO_2 was deposited by sol-gel onto Al_2O_3 microfiltration membranes.
- Coating decreased permeability by 50 and 12% for 200- and 800-nm Al_2O_3 membranes.
- Flow through membrane results in higher reaction rates compared to flow on top.
- Higher *vis* photocatalytic activity for N-doped TiO_2 vs. non-doped TiO_2 membranes.
- Mass transfer is a critical parameter for the design of immobilized PMR.

Abstract

Commercial α-Al_2O_3 photocatalytic membranes with a pore size of 200 and 800-nm were coated with N-doped TiO_2 photocatalytic film using a sol-gel technique for concurrent bottom-up filtration and photocatalytic oxidation. X-ray diffraction confirmed that the deposited films are in the form of anatase. The concentration of N found by X-ray photoelectron spectroscopy was in

the range of 0.3–0.9 atomic percentage with 78–84% coverage. Membrane permeability after coating decreased by 50% and 12% for the 200- and 800-nm membrane substrates, respectively. The impact of operational parameters on the photocatalytic activity (PCA) of the N-doped TiO_2-coated membranes was examined in a laboratory flow cell based on degradation of the model micropollutant carbamazepine, using a solar simulator as the light source. The significant gap in degradation rate between flow through the membrane and flow on the surface of the membrane was attributed both to the hydraulic effect and in-pore PCA. N-doped TiO_2-coated membranes showed enhanced activity for UV wavelengths, in addition to activity under visible light. Experiments of PCA under varying flow rates concluded that the process is in the mass-transfer control regime. Carbamazepine removal rate increased with temperature, despite the decrease in dissolved oxygen concentration.

Keywords: N-doped TiO_2; Water treatment; In-pore degradation; Ceramic membrane; Photocatalytic membrane reactor (PMR)

1. Introduction

The use of semiconductors in combination with sunlight irradiation (i.e. photocatalysis) for the treatment of water and wastewater is classified as a heterogeneous advanced oxidation process. The main limitations of TiO_2 are a relatively wide band gap (3.2 eV for anatase [1]), resulting in about 5% spectral overlap between its absorbance and sunlight emission ($\lambda < \sim 390$ nm), and recombination of the generated electron–hole pairs. Non-metal doping of TiO_2, using N, might produce enhanced UV and visible light (*vis*) activity [2–4]. The isolated narrow N band

formed above the TiO_2 valence band is believed to facilitate *vis* absorption by acting as a stepping stone for excited electrons [5]. While there is some debate on how the activity is increased, this shift may enable the design of solar photocatalytic reactors for water treatment.

Photoreactors operated with slurry photocatalysts may result in catalyst leaching and settling, and require separation/recycling of the catalyst from the treated water which is an inconvenient, time-consuming and expensive process. In addition, light penetration can be limited due to light absorption and scattering by the catalyst. Alternative photoreactors are based on the photocatalyst fixed on various carrier materials at different configurations such as fixed-bed [6,7], rotating-disk [8], falling-film [9], (multi)annular/immersion, optical fiber/hollow tube, monolith, microreactor [10] and photocatalytic membranes [11–15]. In the photocatalytic membrane reactor (PMR) hybrid configuration, the catalyst is embedded, and thus immobilized, in a membrane matrix and activated by direct illumination of the membrane. TiO_2 immobilized on membranes provides photocatalytic degradation and filtration concurrently [16].

Core parameters influencing photocatalytic efficiency are catalyst loading/coated surface area, water pH and quality (organic/inorganic), temperature, dissolved oxygen (DO), contaminant concentration and type, and light intensity [10,17–19]. Moreover, maximized light utilization and mass transfer are critical as immobilization reduces the active surface area and the reactants' contact with the catalyst. As the hydroxyl radicals produced have a very short lifetime, photocatalytic oxidation of pollutants (reactants) will only occur on or close to the surface [20]. For surface reactions, mass transfer may limit the reaction, especially as transport is by diffusion [6,8,21].

Although the use of renewable solar energy is attractive from an energy point of view, most of the PMRs in the literature are activated by UV light [16]. Ke et al. [22] were the first to report

a PMR with *vis* activity using Ag-doped zeolite coated on alumina membranes. These membranes were more efficient than TiO_2 membranes at degrading methylene blue under both UVA (λ = 365 nm) and *vis* (λ > 420 nm). Others have fabricated various vis-activated photocatalytic membranes, demonstrating the degradation of different organic dyes [23–27]. Cao et al. [28] were the first to fabricate C, N-doped TiO_2 membrane on porous alumina support; however, the photocatalytic activity (PCA) was only tested on unsupported films, in batch operation. Nearly complete degradation of methyl orange dye was obtained after four hours irradiation with *vis* light. However, upon excitation, organic dyes have a tendency to act as photosensitizers, making it difficult to attribute their degradation to a purely photocatalytic effect [29]. Photocatalytic degradation of persistent pollutants may prove more environmentally insightful compared to degradation of dye compounds.

In this research, N-doped TiO_2 coatings were deposited via sol-gel on commercial α-Al_2O_3 membranes and characterized for their surface morphology, crystal structure, elemental composition and permeability. Several groups have reported fabrication of ceramic TiO_2/Al_2O_3 composite membranes with a hierarchically porous architecture and photocatalytic activity by sol-gel technique [30–33]. Porosity gradient is used to increase water permeability of the separative layer. Another factor in composite membrane fabrication is the integrity of the active layer to preserve the separation function over time. Choi et al. [30] found that at least three coating layers were needed to prevent cracks and pin-holes in the TiO_2/Al_2O_3 composite membranes. However, ultrafiltration membrane synthesis by sol-gel method allows fabrication of layers with a pore size of up to ~50 nm [34]. The advantage of the proposed herein sol-gel method (pipette “drop-coating”) is the simplicity of applying the coating on a commercially available microfiltration membrane.

To date, there have been no reports on the degradation of environmentally persistent pharmaceutical water relevant contaminant as carbamazepine specifically by an immobilized PMR induced by uv-*vis* light active N-doped TiO_2. The goal of this study was to examine the PCA of immobilized N-doped TiO_2 membranes by following carbamazepine (CBZ) degradation, and to determine the impact of physical and operational parameters such as operation mode (surface vs. in-pore PCA), wavelength dependence, flow rate and temperature on the PCA. CBZ is a widely used antiepileptic drug that is known to resist degradation in conventional water and wastewater treatments [35,36].

2. Experimental

2.1. Materials and reagents

A CBZ standard (>99% purity) was obtained from Sigma-Aldrich and LC–MS-grade methanol and water were sourced from Bio-Lab Ltd. (Jerusalem, Israel). All chemicals were used as obtained and a stock solution of CBZ was prepared by dissolving it in deionized (DI) water (Direct-Q3 UV system, Millipore-France) at a concentration of 50 mg l^{-1}. Stock solutions of sodium phosphate monobasic (12 g NaH_2PO_4 in 1 l water) and sodium phosphate dibasic (14.2 g Na_2HPO_4 in 1 l water) from Sigma Aldrich (Germany) were used together to make a pH 7 buffer.

2.2. Preparation of N-doped TiO_2 thin-film coatings on membranes

Commercial flat α-Al_2O_3 microfiltration membranes with a nominal pore size of 200 and 800 nm (Nanostone Water, formerly KSM Water GmbH) were selected as the substrates for the N-doped TiO_2 coating. The membrane sheets were cut to give an effective filtration area of 2.2 x 4.2 cm^2, with a thickness of 6.6 and 3.8 mm for the 800- and 200-nm membranes, respectively.

N-doped TiO_2 coatings were prepared by sol-gel deposition as previously described [37,38]. Briefly, tetrabutyl orthotitanate and triethanolamine were dissolved in isopropanol followed by vigorous stirring for few minutes. Then ammonium hydroxide was added and the solution was vigorously stirred for 30 min at room temperature. Before the solution was deposited, the substrates were carefully cleaned by ultrasonic treatment with citric acid (0.1 M, at 80 °C) and then acetone (at room temperature), and finally air-dried for 24 h. The N-doped TiO_2 coatings were applied by a drop-coating method using a pipette (2.5 ml corresponding to 0.12 ml cm^{-2} of membrane area). A 1 ml of solution was deposited at the sample center using a graduated Eppendorf pipette. The solution quickly spread out on the surface forming a homogeneous film. In a few seconds it is absorbed. Afterwards another 1 ml of solution was deposited in the same manner and finally, the last 0.5 ml was deposited, followed by annealing at 450 °C for 1 h. Preparation of non-doped TiO_2 coatings followed a previously described procedure [38].

2.3. Membrane characterization

2.3.1. Surface analysis

X-ray photoelectron spectroscopy (XPS) analysis was carried out using a ThermoFisher Scientific Thetaprobe spectrometer with Al Kα monochromated radiation at a power of 140 W, spot size of 400 μm and a take-off angle of 37º (relative to the surface normal). Survey spectra

were acquired using a 0.4-eV channel width, 50 ms channel^{-1}, 0–1350-eV spectrum width, 2 scans, and a pass energy of 300 eV. The high-resolution XPS spectra of individual elements were acquired using a 0.2-eV channel width, 50 ms channel^{-1}, 50 eV pass energy. The aliphatic C peak at 285.0 eV was used as a binding-energy reference. Curve fitting was performed with the ThermoFisher Scientific Avantage software after subtraction of a Shirley background and quantification using the instrument-modified Wagner sensitivity factors. Coverage of the Al_2O_3 substrate by the TiO_2 film was calculated from the atomic percentages (at.%) of titanium and aluminum, and normalized by the atomic densities in the two solids, as detailed in Grilli et al. [39].

2.3.2. Permeability

The membrane ~~water~~ permeability for water was determined by measuring the pure water flux in a pressure-step test experiment. N_2 (99.999%) was used to force DI water from a 5-l holding tank into the membrane pressure cell, operated in ~~by~~ dead-end filtration mode. The accumulated permeate water weight with time was recorded by the Balint software and the clean water flux was calculated (Eq. 1). A pressure regulator (Precision, SMC, Japan) was used to keep the pressure constant throughout the experimental procedure. The temperature of the filtered water was monitored by a thermocouple (Rapid Inc., UK).

$$J_w = \frac{\Delta m}{\rho \Delta t A} \quad (1)$$

where A is the membrane surface area and ρ is the water density.

2.4. Photocatalytic activity test of N-doped TiO_2-coated Al_2O_3 membrane

The PCA of the coated membranes was determined with a custom-made, versatile PMR for concurrent filtration and solar photocatalytic degradation as detailed in Fig. 1. The flow cell was a laboratory-scale system ~~for concurrent filtration and solar photocatalytic degradation~~ used in recirculating ~~semi-~~batch ~~operation~~ mode, operated in two flow configurations (FC), schematically shown in Fig. 1 as FC1 and FC2, and placed under light from a solar-simulator. The filtered and irradiated area of the filtration cell was 2.2 x 4.2 cm^2. A quartz cover was placed above the membrane to ensure a uniform water height of 6.5 mm above the membrane and to seal the chamber. A 200-ml feed solution of 1 mg l^{-1} CBZ (4.24 x 10^{-3} mM, pH 7) was recirculated through the system for 30 min to ensure an adsorption/desorption equilibrium of CBZ on the membrane in the dark prior to irradiation. In the FC1 flow configuration, the feed solution was ~~then~~ filtered from the bottom up (i.e. uncoated) to the photocatalytically coated side of the membrane in a dead-end filtration mode. Hence, only the permeate was exposed to the photocatalytic effect. Treated water was collected on the permeate side and pumped back into the feed bottle, for a total irradiation time of 2 h. The advantage of filtering from the support side is that the photocatalytic layer is less exposed to surface fouling, which may shade the photocatalytic effect. Only molecules smaller than the pore size will pass to the permeate side and consequently be subjected to the photocatalytic degradation. The reasoning for the flow direction to the PMR can be found in Appendix A. In the FC2 flow configuration, the feed water flowed on the coated membrane surface without membrane permeation. The filtration flow during the experiments was driven by a peristaltic pump with the exception of the Al_2O_3 membrane with a pore size of 200 nm. For these membranes, the feed solution was driven through the membrane by compressed air, connected to a sealed feed bottle at a pressure

corresponding to the desired flow rate. The dilution ratio in the experimental system (i.e. illuminated volume vs. total volume) was 0.04.

A solar simulator was used as the light source to ensure controlled irradiation conditions for the PCA experiments. A 300-W ozone-free xenon arc lamp was used with a 1.5 Global air mass (AM) filter (Newport, full spectrum 300 W, 50.8 mm x 50.8 mm, USA). Incident spectral irradiance before each experiment was measured by a spectroradiometer (International Light, ILT 900R, USA). The integrated incident irradiance was 1.4, 55.0 and 712.3 W m^{-2} for the UVB (280 nm–320 nm), UVA (320 nm–400 nm) and *vis* (400 nm–700 nm) ranges, respectively. The PMR's efficiency was also tested using two long-pass (LP) filters (Newport, USA) which allowed screening out specific wavelengths: (i) all wavelengths below 320 nm (320LP~~λ >320 nm~~); (ii) all wavelengths below 400 nm (400LP~~ λ >400 nm), (iii) all wavelengths below > 280 nm (no LP filter) (λ >280 nm)~~. The temperature was measured using a type T thermocouple connected to a dual-input thermometer (CHY 502A, Taiwan) submerged in the feed water and inserted into the irradiated chamber. The oxygen concentration inside the feedwater chamber was monitored using a DO meter (WTW Multi 3410, Germany).

Fig. 1

2.5. Chemical analysis

The CBZ concentration was determined by high-performance liquid chromatography (HPLC) (Agilent, model 1100), using a phenyl reverse-phase column (ACE-RP, 2.1 mm × 250 mm, 5 μm). The mobile phase consisted of water (A) and methanol (B) and the detection

wavelength was 286 nm. The flow rate was specificied to be 0.5 ml min^{-1}, the temperature set to 40 ºC, and the injected volume 100 µl. The mobile-phase eluent gradient started with 60% of eluent A, followed by a 2 min linear gradient to 10% eluent A, 4 min isocratic elution and a 2 min linear gradient back to 60% eluent A, maintained for 5 min to equilibrium.

3. Results and Discussion

3.1. Membrane characterization

3.1.1. Surface characterization of the N-doped TiO_2-coated membranes

The deposited film did not have a structure which was clearly distinguishable by SEM micrographs from the substrate membrane (Fig. A.1 and A.2). The XRD patterns for the N-doped TiO_2-coated membranes (Fig. A.3) confirmed that the films deposited on the two membranes are in the form of anatase, as shown by the intense (101), (103), (112), (200), (105) and (211) peaks. The average grain size, calculated from the (200) peak, was 12 nm for the 200-nm membrane and 17 nm for the 800-nm membrane. The other XRD peaks corresponded to Al and Zr, plus a mixed Al/Zr oxide phase, as seen for the uncoated membranes (Fig. A.3).

The surface elemental composition of both of the N-doped TiO_2-coated membranes obtained by XPS analysis is given in

Table 1. The different Al concentrations for the 200- and 800-nm membranes confirmed that the film is not continuous in either case, leaving some of the membrane exposed. The surface coverage was estimated based on the XPS Ti and Al concentrations [39]. The surface-coverage values calculated in this manner do not take into account any local variations in the thin-film coverage or the specific active surface area exposed (e.g. due to high surface roughness or porous structure). The surface roughness could lead to an over-estimation of the N-doped TiO_2 coverage, as a result of shadowing of the incoming X-ray beam and obstruction of outgoing electrons by the coating. Hence, the limitations of this approach should be noted; nevertheless, assuming the roughness of the samples is similar, it provides a useful indicator of relative surface coverage between the coatings deposited on the different membranes. The results show that there is an approximate N-doped TiO_2 surface coverage of 84% for the 200-nm membrane and 78% for the 800-nm membrane. Hence, there is no substantial difference in coverage as the membrane pore size increases, but the slightly higher coverage for the 200-nm membrane might be explained by a greater loss of sol-gel solution through the larger pores of the 800-nm membrane.

There is no obvious method of depositing a ‘uniform’ sol-gel layer onto a substrate which exhibits an extreme surface morphology due to its high porosity. This coverage will not be 100 % conformal, but since the sol-gel annealing process will also lead to cracks appearing in the coating, this is not considered to be a substantial drawback. This process is performed just one time, so there was no intention to build up the coating thickness through repeating this process in a ‘multi-layer’ fashion. In order to build a thicker film on the membrane surface, a quick and low temperature annealing process would have to be performed after each deposition to allow a solidification of each film. However, the permeability would be strongly affected. Results of this study showed that applying the more conventional dip-coating technique produced substrates

with poorer uniformity while the drop-coating resulted in a better uniformity and is easily applied, even for larger surfaces, while dip-coating requires higher solution volume.

The N 1s photoelectron peaks for both membranes are shown in Fig. 2. The spectra can be fitted with three or four peaks, contributing 0.1–0.3 at.% each (plus one peak for the Mo 3d transition for the 200-nm membrane only). Assignment of N peaks is not straightforward and there is disagreement in the literature regarding this issue. However, it is generally accepted that the peak at approximately 396 eV corresponds to N substituting O in the TiO_2 phase. Baker et al. [40] recently showed that the peak at approximately 400 eV is present on many surfaces due to the presence of N-containing organic contamination, but a peak at a similar binding energy can also occur due to the presence of interstitial NO^- species in the bulk [41]. Furthermore, the peak at approximately 402 eV is associated with surface contamination [40]. It should be noted that on the uncoated surfaces, the N 1s peak for both the 200-nm and 800-nm membranes had only two components, at approximately 400 and 402 eV (~~data not shown~~ exemplified for 800-nm membrane in Fig.A.5). The final component, at approximately 398 eV, most probably corresponds to interstitial N in the TiO_2 phase [42]. Hence, in the thin N-doped TiO_2 film on the 200-nm membrane, N is present as both substitutional and interstitial N (and possibly interstitial NO^-), whereas in the thin film formed on the 800-nm membrane, the N is present as interstitial N (and possibly NO^-). The reason for the different doping of the thin films on the different substrates is not known, but may be associated with different behavior/evolution of the sol-gel molecular structure when deposited onto the membranes with different pore sizes. Traces of other metals were detected as contaminants.

3.1.2. Permeability

Permeability of the 200-nm and 800-nm membranes was measured to evaluate the integrity and properties of the membranes before and after deposition of N-doped TiO_2 film. Fig. 3a and 3b show the pure water flux as a function of pressure for the 200- and 800-nm membrane, respectively. The data shows a linear dependence and the water permeability is given by the gradient of the line. The pure water permeability for the uncoated 200-nm membrane was 3800 ± 17% L m^{-2} h^{-1} bar^{-1} (LMH bar^{-1}), and 1900 ± 15% LMH bar^{-1} for the coated membrane. For the uncoated 800-nm membrane, the water permeability was 21,000 ± 6% LMH bar^{-1}, and 18,500 ± 4% LMH bar^{-1} for the coated membrane. The membrane permeability decreased by ~50% after coating deposition for the 200-nm, while in the case of 800-nm, this decrease was ~12%. Choi et al. [43] also investigated the permeability for sol-gel deposited TiO_2 films onto 100 nm pore size Al_2O_3 membrane substrates and reported similar results. They reported a continuous reduction in membrane permeability as a function of coating layers, with a 40% decrease in permeability for three coating layers, corresponding to a coating thickness of ~0.9 μm. To summarize, sol-gel N-doped TiO_2 thin films were not distinguishable in the SEM micrographs for either membrane. However, the sol-gel solution has clearly penetrated the membrane pores and due to accumulation may cause a partial blockage. This phenomenon was confirmed by a significant decrease in the permeability of those membranes. The 800-nm membrane substrates showed an insignificant loss in permeability, this improvement in performance probably being due to a more uniform distribution and thickness of the sol-gel coating within the pores.

3.2. Surface recirculation on top versus through the photocatalytic membrane

One of the key reasons for using membranes as a coating substrate is the possibility of increasing PCA due to enhanced contact between pollutant and surface. The effect of recirculating through the photocatalytic membrane (filtration, FC1) as opposed to recirculating the water on the surface of the photocatalytic membrane (FC2) was examined (Fig. 4). The overall degradation rate of CBZ was represented by a first-order kinetic model (Eq. 2) for the case of low pollutant concentration. Under the experimental conditions, CBZ degradation with time followed first-order kinetics with a regression coefficient above 99% (data not shown).

$$r_0 = \left[\frac{V_t}{A_{irr}}\right]\left[-\frac{dC_b}{dt}\right] = k_0 C_b \qquad (2)$$

where V_t is the total water volume and A_{irr} is the external area of the irradiated catalyst, C_b is the pollutant concentration in the bulk, k_o is the first-order observed rate constant.

Integration of Eq. 2 (with the restriction of $C = C_0$ at $t = 0$, with C_0 being the initial concentration in the bulk solution and t the reaction time) will lead to the following relation:

$$k_0' = ln\left(\frac{C_b}{C_0}\right)/t \qquad (3)$$

where k_o' is the observed first-order rate constant normalized by irradiated catalyst area to total volume ratio.

Direct photodegradation of CBZ (using uncoated Al_2O_3 membranes) after 120 min exposure was negligible (<1%, Fig.A.7). CBZ showed negligible adsorption to the N-doped TiO_2-coated membranes in the dark. After 120 min irradiation, both 200-nm and 800-nm coated membranes showed similar CBZ-degradation rates for flow through the membrane, with observed rate constants of 0.0087 ± 0.0005 and 0.0089 ± 0.0009 ~~l m^{-2}~~ min^{-1}, respectively. These values correspond to 125 ± 9 mg m^{-2} specific CBZ removal (i.e. the cumulative CBZ removal per

unit area of membrane) by the PMR within the 120 min experimental time (see Fig. 4 inset on the right). Recirculating the CBZ solution on the surface of the membranes (i.e., without membrane permeation) resulted in the rate constant being substantially reduced (by ~90%). ~~One reason for this difference is improved mixing of the water on the coated membrane surface caused by the flow through the porous material, increasing the contact of molecules with active sites and therefore decreasing the mass-transfer limitation. However, t~~The significant gap in degradation rate between flow through the membrane and flow ~~on the surface of the~~ without membrane permeation cannot be attributed to the hydraulic effect alone and probably arises from in-pore PCA. It is impossible to determine the exact surface area available for PCA for a complex structure of the asymmetric membrane; however, this hypothesis can be logically elucidated. When a system is operating with feed water flowing on the coated surface (water height 6.5 mm), only the molecules at close proximity to the surface (i.e. in the boundary layer) can react at the active sites. The molecules can reach the surface either by diffusion or by dispersion due to complex flow pattern resulting from extreme membrane surface morphology. Molecules flowing outside the boundary layer will by-pass the photocatalytic process and result in the observed low efficiency. However, membrane permeation provides a more effective contact between the reactants and the catalytically active sites by introducing forced transport of reactants by convection inside owing to membrane high tortuosity. In this configuration, the molecules are flowing in a channel at an average distance of ~400 nm (e.g. for the 800 nm membrane) from the channel wall. Therefore, the interaction of molecules with active sites inside the pores is more probable. This configuration allows one to minimize the mass transfer resistances between the bulk of the fluid and the active surface. As a consequence of the forced transport of reactants by convection inside the pores, in addition to transport by diffusion, an

increased reaction rate can be achieved. Therefore, the most plausible explanation for the significant increase in pollutant degradation is the additional utilization of the coated pore walls (in a thin upper layer). ~~The photons emitted from the solar simulator are collimated and therefore if the membrane had an ideal porous body with cylindrical and parallel pores, the photons would pass through the membrane without excitation of the pore walls. In this case, the active surface area could be estimated as the external surface area subtracting the voids. However, the membrane in this work has an asymmetric pore structure hence the photons can be absorbed by the pore walls and contribute to the PCA.~~ Although it is impossible to directly calculate the radiative transfer at a local scale; however, a porous material cannot be considered as not penetrable to radiation. The radiation is anticipated to gradually absorb and scatter in the material as a function of the porous structure. Thus, the total PCA of a PMR configuration is divided to surface and in-pore PCA as can be seen in the pie chart of Fig. 4 inset where surface PCA component is responsible for only ~10% out of total PCA.

The results presented here are consistent with the results reported by Tsuru et al. [44], who used a photocatalytic membrane for decomposition of methanol (during gas filtration) and found that it was more efficient when operated in a filtration mode compared to just surface flow. Wang et al. [14] also demonstrated a lower decomposition rate of Acid Red 4 for cross-flow versus dead-end operation using TiO_2 supported on a porous ceramic tube. They attributed the effect to poor mechanical mixing, a lower contacting surface area and stagnant regions above the membrane.

The difference in N doping between coated 200- and 800-nm membranes (section 3.1.1) did not seem to affect the PCA. The coated 200- and 800-nm membranes were comparable in terms of CBZ degradation. However, the permeability tests reported in section 3.1.2 showed a

reduction in the permeability by ~50% for the coated 200-nm membrane. Hence, these membranes may function less well in a low-pressure system (i.e., max pressure 0.5 bar) when fouling and cake formation are taken into account. Based on the results shown here, it is clear that N-doped TiO_2 coating should be deposited onto an Al_2O_3 membrane with a sufficient pore size (800 nm here) to enable sufficient hydraulic permeability. Consequently, the physical and operational parameters were examined for the N-doped TiO_2-coated 800-nm Al_2O_3 membranes.

3.3. Visible light activity of the N-doped TiO_2- versus TiO_2-coated membranes

The effect of different wavelengths on the PCA of N-doped TiO_2 versus TiO_2 was examined using two LP filters inserted into the solar simulator. Specifically, the examined wavelength ranges were: $\lambda > 280$ nm (no filter, full spectrum), $\lambda > 320$ nm (UVA + *vis*) and $\lambda > 400$ nm (*vis*). The transmittance for the solar simulator incident irradiation (with and without the selected filters) as a function of wavelength is given in Fig. A.8. Fig. 5 presents the CBZ-degradation rate constant under the full spectrum, UVA + *vis* and *vis* by the two coating types. When applying the full spectrum, the N-doped TiO_2-coated membranes produced a significantly higher (by > 100 %) degradation rate than undoped TiO_2-coated ones, with rate constants of 0.0085 ± 0.0004 ~~l m^{-2}~~ min^{-1} and 0.0040 ± 0.0007 ~~l m^{-2}~~ min^{-1}, respectively. The dependence of TiO_2 and N-doped TiO_2 on wavelength is best understood by the contribution of each spectral range to the total degradation of CBZ, as summarized in

Table 2. While the UVB and UVA parts of the spectrum make equal contributions to TiO_2 activity, most of the N-doped TiO_2 activity is contributed by UVA. Finally, only the N-doped TiO_2-coated membranes showed PCA in the visible region, with this visible light contributing 17% of the total activity, as opposed to TiO_2 which was within the limit of measurement error and could therefore be regarded as negligible.

The UVB photons have energy greater than the TiO_2 band-gap and can hence directly promote electrons to excited states of the conduction band. These states show a lower electron–hole recombination rate in comparison to those excited by photons in the UVA range [45]. Hence the reduction in degradation rate when filtering out UVB wavelengths was expected, even though it constituted only ~2% of the total UV radiation. However, doping TiO_2 with N is assumed to reduce recombination [46]. Therefore, more efficient utilization of wavelengths in the UVA range resulted in enhanced efficiency. Wang et al. [46] proposed that the *vis* activity of N-doped TiO_2 originates from single-electron-trapped oxygen vacancy intrabands, while the dopant N atoms/species function to prevent photoinduced electrons and holes from recombining.

The enhanced UV–*vis*-driven PCA of N-doped TiO_2 has been confirmed in many studies, although the origin of this activity is subject to debate. Asahi et al. [2] claimed that the doped N atoms act to narrow the band gap of TiO_2, making it capable of absorbing visible light and hence exhibiting *vis*-driven photocatalysis. Irie et al. [3] argued that an isolated narrow band is formed above the valence band which is responsible for the visible response by promoting electrons from this interband state to the conduction band. However, Ihara et al. [47] insisted that it is only oxygen vacancies that contribute to the *vis* activity and that the doped N atoms only enhance the stabilization of these oxygen vacancies. Mohamed et al. [48] has reported on the enhanced photocatalytic response of N-doped TiO_2 nanorods assembled microspheres towards phenol degradation under UV and *vis* light irradiations. In contrast, the undoped TiO_2 samples were able to degrade phenol under UV light alone. Larumbe et al. [49] conducted a comparative study on undoped, N and Fe doped TiO_2 nanoparticles and found 0.3%N-doped TiO_2 as superior for methyl orange degradation under both UV and *vis* light. Increase in N content in the samples to 0.7% displayed poor response under both UV and *vis* light in spite of the reduction in estimated

band-gap energy. In contrast to Wang et al. [46], the negative effect of increasing N content was assigned to the increase in oxygen vacancies acting as recombination centers.

3.4. Flow-rate dependence

The effect of flow rate on PCA was examined by recirculating the water inside the system at different flow rates. Once the catalyst is activated by the incident light, maximum contact between the active sites and the target molecules must be achieved. Hence, the mass-transfer limitation between molecules in the fluid and solid catalytic surface must be considered. In external mass transfer, the target pollutant must diffuse from the bulk fluid to the photocatalytic surface where it is adsorbed and it reacts, while internal mass transfer can be neglected for the case of thin films. The observed degradation-rate constant in fact includes mass transfer and intrinsic kinetic reaction-rate constants according to the correlation in Eq. 4 [50–52]. However, finding the various coefficients were not the focus of this work.

$$\frac{1}{k_0} = \frac{1}{k_r K} + \frac{1}{k_m} \qquad (4)$$

where k_r is the reaction-rate constant, K is the Langmuir–Hinshelwood (L–H) adsorption coefficient, k_m is the external mass-transfer coefficient.

The effect of increasing flow rate on CBZ degradation rate was examined at 0.5, 1, 4 and 8 l h^{-1} (Fig. 6). The CBZ degradation-rate constant increased with increasing flow rate, thereby confirming that the process is in the mass-transfer control regime. The increase in the degradation rate constant reached a maximum value at 4 l h^{-1}, followed by a decrease and greater variation at 8 l h^{-1}. This decrease at high flow rates was not expected since the reaction-rate

constant would have been expected to further increase or reach a plateau when the reaction was no longer diffusion-limited. However, at high flow rates, physical factors that depend on the properties of the membrane can affect the reaction rate. A possible explanation for the observed behaviour is an increase in membrane resistance with increasing velocity, causing the water to randomly bypass the more densely coated pore channels resulting in a reduction in the active area. Hence, the substrate properties play a crucial role in process planning and optimization of performance.

Similar results were found by Lin and Valsaraj [53], who used a photocatalytic reactor made up of a ceramic multichannel monolith as a support for TiO_2 and monitored the degradation of o-dichlorobenzene and phenanthrene. The effect of water-flow velocity was investigated and the operation was shown to be in the mass-transfer control regime. Therefore, increasing the flow velocity, and thus the Re number, could reduce the external-mass-transfer resistance. Duran et al. [21] used a test setup that allowed flow along the photocatalytic surface. The mass-transfer limitation disappeared at $Re > 2600$, i.e., when the flow was no longer laminar.

For the case of a batch operated system, increasing photocatalytic efficiency can be achieved through improved mass transfer of the pollutant to the coated surface using higher flow rate. However, the additional operational costs must be weighed in relation to the increase in process efficiency. For the case of a system operated in a continuous mode (e.g. as a plug flow reactor), elongation of the residence time (i.e. lower permeate flux) enhances the degradation efficiency of organic pollutants and leads to an improvement of permeate quality. As photocatalytic efficiency of immobilized systems is still limited by the available photocatalytic

active area, longer residence time may not be a sufficient solution, hence introducing a circulation stream with flux increase can still be a viable option.

3.5. Temperature effect on PCA

Permeate flowing in a thin layer (e.g. a few millimeters) above the membrane can be subjected to significant temperature changes. It is therefore important to examine the impact of temperature on PCA. Temperature effects on the photocatalytic reaction have been detailed by Herrmann [54]. In general, the sequence of steps involved in converting reactants to products is: (1) transfer of the reactant from the bulk fluid to the catalytic surface; (2) adsorption of the reactant at the catalytic surface; (3) reaction in the adsorbed phase; (4) desorption of adsorbed product(s); (5) transfer of the products from the solid into the bulk fluid. Although the photocatalytic process is triggered by photonic activation, and does not require heating, the observed first-order rate constant still depends on temperature through the L–H adsorption coefficient K (Eq. 4), which varies with temperature according to van't Hoff's law [29].

This effect was examined by heating or cooling the feed solution using a temperature-controlled circulating water bath (MRC BL-30, Israel). The temperature was set to 20 ^{o}C or 45 ^{o}C and the flow rate was set to 1 l h^{-1}. The temperature and the DO concentration were monitored throughout the irradiation experiment. The initial DO values at 20 °C and 45 °C were 9.4 and 6.7 mg l^{-1} respectively, as an increasing temperature resulted in a decrease in the initial DO concentration due to the reduced solubility of O in water (Fig. A.9). Furthermore, a small decrease in DO concentration (<10%) was observed after 30 min for both temperatures and then

remained constant, suggesting that O adsorption to the catalyst had reached saturation. Thus, the concentration of O is not necessarily a limiting factor at these temperatures. O does not seem to compete with other dissolved species during the adsorption on TiO_2 since oxidation and reduction occur at different locations [55]. Moreover, DO acts as an electron acceptor and therefore decreases electron–hole recombination on the catalyst and also may be involved in the formation of other oxidative species (e.g. superoxide, hydrogen peroxide).

The experiment performed at 45 °C resulted in ~40% increase in the degradation-rate constant compared to the experiment performed at 20 °C (Fig. 7). This result is in good agreement with the theory described above. The CBZ stability at 45 °C was examined by repeating the experiment using an uncoated membrane, which showed a negligible effect within error limits. The lower DO concentration at 45 °C did not result in a reduction of the CBZ-degradation rate, suggesting that the adsorption/desorption equilibrium of CBZ is a more significant limiting factor than DO. Similar results have been reported in the literature. Mozia et al. [56] found a linear correlation between the photocatalytic degradation-rate constant of the azo dye, Acid Red 18, at reaction temperatures in the range of 20–60 °C. Increasing the temperature from 20 °C to 50 °C resulted in a 17.5% increase in the reaction rate, whereas above 60 °C, a decrease was observed. They also observed that although the DO concentration in the water decreases with increasing reaction temperature, the effectiveness of the photocatalytic degradation increases. A similar relationship was obtained by Chen and Ray [57], who attributed the increase in the rate constant for a temperature rise of 10 °C to 50 °C to the increasing collision frequency of molecules in solution.

4. Conclusions

Highly efficient UV–*vis*-active N-doped TiO_2 coatings were successfully deposited by sol-gel (using pipette "drop-coating" method) onto commercial Al_2O_3 microfiltration membranes. Surface characterization revealed a coating with anatase structure and N content in the range of 0.3–0.9 at.%, predominantly located at interstitial sites in the TiO_2. Good surface coverage (~80%) was achieved by the proposed method. Using commercial microfiltration membrane as a substrate for a thin film coating, instead of building an independent separative layer, does not significantly compromise membrane permeability and will still allow operation at low transmembrane pressure. However, as applied as a single layer, coating's integrity under continuous operation in field conditions must be evaluated.

The porous structure of the membrane can provide a significant improvement in PCA compared to smooth coated surfaces. Recirculating the treated water through the photocatalytic membrane (filtration) resulted in a significantly higher (by ~90%) CBZ reaction rate, this was attributed to "in-pore" PCA due to increased contact of molecules with the active sites caused by the flow through the porous material. More importantly, N-doped TiO_2 Al_2O_3 membranes were especially active under UVA and possess *vis* PCA which accounts for 17% of the total PCA, allowing more efficient utilization of solar light. The CBZ-removal rate increased with temperature, despite the decrease in DO concentration. A disadvantage of coated PMRs is that the effective water cleaning process is controlled by diffusion of pollutants to the catalytic surface. Increasing the mass transfer via an increase in water flux was found to be limited by membrane properties. Yet, optimization through elongation of the process residence time should be considered due to the

additional operational costs of increasing water flux to the system. While planning a full scale system, a threshold for a degradation of a standard pollutant should be introduced for quantification of all available options.

Acknowledgments

This research received funding from the European Union's Seventh Framework Programme, FP7, under grant agreement no. 245513-2 ("NATIOMEM: nano-structured N-doped TiO_2 photocatalytic membranes for water treatment" collaborative project). We would like to thank Ole Grønborg from ULTRAAQUA (Denmark) for planning and building the flow-cell prototype, and the project coordinator Gerald Heinicke from DHI (Denmark). We would also like to thank Ann Dorrit Enevoldsen from DHI (Denmark) for her contribution to this research and assistance in editing this paper.

References

[1] O. Carp, C.L. Huisman, A. Reller, Photoinduced reactivity of titanium dioxide, Prog. Solid State Chem. 32 (2004) 33–177.

[2] R. Asahi, T. Morikawa, T. Ohwaki, K. Aoki, Y. Taga, Visible-light photocatalysis in nitrogen-doped titanium oxides., Science. 293 (2001) 269–271.

[3] H. Irie, Y. Watanabe, K. Hashimoto, Nitrogen-concentration dependence on photocatalytic activity of $TiO_{2-x}N_x$ powders, J. Phys. Chem. B. 107 (2003) 5483–5486.

[4] C. Di Valentin, E. Finazzi, G. Pacchioni, A. Selloni, S. Livraghi, M.C. Paganini, E. Giamello, N-doped TiO_2: Theory and experiment, Chem. Phys. 339 (2007) 44–56.

[5] M. Pelaez, N.T. Nolan, S.C. Pillai, M.K. Seery, P. Falaras, A.G. Kontos, P.S.M. Dunlop, J.W.J. Hamilton, J.A. Byrne, K. O'Shea, M.H. Entezari, D.D. Dionysiou, A review on the visible light active titanium dioxide photocatalysts for environmental applications, Appl. Catal. B Environ. 125 (2012) 331–349.

[6] M.F.J. Dijkstra, H. Buwalda, a. W.F. De Jong, A. Michorius, J.G.M. Winkelman, a. a C.M. Beenackers, Experimental comparison of three reactor designs for photocatalytic water purification, Chem. Eng. Sci. 56 (2001) 547–555.

[7] A.J. Feitz, B.H. Boyden, T.D. Waite, Evaluation of two solar pilot scale fixed-bed photocatalytic reactors, Water Res. 34 (2000) 3927–3932.

[8] D.D. Dionysiou, M.T. Suidan, I. Baudin, J.-M. Laîné, Oxidation of organic contaminants in a rotating disk photocatalytic reactor : reaction kinetics in the liquid phase and the role of mass transfer based on the dimensionless Damköhler number, Appl. Catal. B Environ. 38 (2002) 1–16.

[9] S. Brosillon, L. Lhomme, D. Wolbert, Modelling of a falling thin film deposited photocatalytic step reactor for water purification: Pesticide treatment, Chem. Eng. J. 169 (2011) 216–225.

[10] T. Van Gerven, G. Mul, J. Moulijn, A. Stankiewicz, A review of intensification of photocatalytic processes, Chem. Eng. Process. Process Intensif. 46 (2007) 781–789.

[11] C.P. Athanasekou, S. Morales-Torres, V. Likodimos, G.E. Romanos, L.M. Pastrana-Martinez, P. Falaras, D.D. Dionysiou, J.L. Faria, J.L. Figueiredo, A.M.T. Silva, Prototype composite membranes of partially reduced graphene oxide/TiO_2 for photocatalytic ultrafiltration water treatment under visible light, Appl. Catal. B Environ. 158-159 (2014) 361–372.

[12] R.E. Morris, E. Krikanova, F. Shadman, Photocatalytic membrane for removal of organic contaminants during ultra-purification of water, Clean Technol. Environ. Policy. 6 (2004) 96–104.

[13] G.E. Romanos, C.P. Athanasekou, F.K. Katsaros, N.K. Kanellopoulos, D.D. Dionysiou, V. Likodimos, P. Falaras, Double-side active TiO_2-modified nanofiltration membranes in continuous flow photocatalytic reactors for effective water purification., J. Hazard. Mater. 211-212 (2012) 304–316.

[14] W.-Y. Wang, A. Irawan, Y. Ku, Photocatalytic degradation of Acid Red 4 using a titanium dioxide membrane supported on a porous ceramic tube, Water Res. 42 (2008) 4725–4732.

[15] H. Dzinun, M.H.D. Othman, A.F. Ismail, M.H. Puteh, M.A. Rahman, J. Jaafar, Photocatalytic degradation of nonylphenol by immobilized TiO_2 in dual layer hollow fibre membranes, Chem. Eng. J. 269 (2015) 255–261.

[16] X. Zhang, D.K. Wang, J.C. Diniz da Costa, Recent progresses on fabrication of photocatalytic membranes for water treatment, Catal. Today. 230 (2014) 47–54.

[17] V.C. Sarasidis, K. V. Plakas, S.I. Patsios, A.J. Karabelas, Investigation of diclofenac degradation in a continuous photo-catalytic membrane reactor. Influence of operating parameters, Chem. Eng. J. 239 (2014) 299–311.

[18] M.N. Chong, B. Jin, C.W.K. Chow, C. Saint, Recent developments in photocatalytic water treatment technology: A review, Water Res. 44 (2010) 2997–3027.

[19] S. Mozia, Photocatalytic membrane reactors (PMRs) in water and wastewater treatment. A review, Sep. Purif. Technol. 73 (2010) 71–91.

[20] C. Minero, F. Catozzo, E. Pelizzetti, Role of adsorption in photocatalyzed reactions of organic molecules in aqueous titania suspensions, Langmuir. 8 (1992) 481–486.

[21] J.E. Duran, F. Taghipour, M. Mohseni, Evaluation of model parameters for simulating TiO_2 coated UV reactors, Water Sci. Technol. 63 (2011) 1366–1372.

[22] X. Ke, S. Ribbens, Y. Fan, H. Liu, P. Cool, D. Yang, H. Zhu, Integrating efficient filtration and visible-light photocatalysis by loading Ag-doped zeolite Y particles on filtration membrane of alumina nanofibers, J. Memb. Sci. 375 (2011) 69–74.

[23] C.P. Athanasekou, N.G. Moustakas, S. Morales-Torres, L.M. Pastrana-Martínez, J.L. Figueiredo, J.L. Faria, A.M.T. Silva, J.M. Dona-Rodriguez, G.E. Romanos, P. Falaras, Ceramic photocatalytic membranes for water filtration under UV and visible light, Appl. Catal. B Environ. (2014).

[24] N.G. Moustakas, F.K. Katsaros, A.G. Kontos, G.E. Romanos, D.D. Dionysiou, P. Falaras, Visible light active TiO_2 photocatalytic filtration membranes with improved permeability and low energy consumption, Catal. Today. 224 (2014) 56–69.

[25] Y. Gao, M. Hu, B. Mi, Membrane surface modification with TiO_2–graphene oxide for enhanced photocatalytic performance, J. Memb. Sci. 455 (2014) 349–356.

[26] C.P. Athanasekou, G.E. Romanos, F.K. Katsaros, K. Kordatos, V. Likodimos, P. Falaras, Very efficient composite titania membranes in hybrid ultrafiltration/photocatalysis water treatment processes, J. Memb. Sci. 392-393 (2012) 192–203.

[27] S. Ma, J. Meng, J. Li, Y. Zhang, L. Ni, Synthesis of catalytic polypropylene membranes enabling visible-light-driven photocatalytic degradation of dyes in water, J. Memb. Sci. 453 (2014) 221–229.

[28] X. Cao, W. Jing, W. Xing, Y. Fan, Y. Kong, J. Dong, Fabrication of a visible-light response mesoporous TiO_2 membrane with superior water permeability via a weak alkaline sol-gel process., Chem. Commun. (Camb). 47 (2011) 3457–3459.

[29] J.-M. Herrmann, Photocatalysis fundamentals revisited to avoid several misconceptions, Appl. Catal. B Environ. 99 (2010) 461–468.

[30] H. Choi, E. Stathatos, D.D. Dionysiou, Sol-gel preparation of mesoporous photocatalytic TiO_2 films and TiO_2/Al_2O_3 composite membranes for environmental applications, Appl. Catal. B Environ. 63 (2006) 60–67.

[31] R. Goei, Z. Dong, T.-T. Lim, High-permeability pluronic-based TiO_2 hybrid photocatalytic membrane with hierarchical porosity: Fabrication, characterizations and performances, Chem. Eng. J. 228 (2013) 1030–1039.

[32] R. Goei, T.T. Lim, Ag-decorated TiO_2 photocatalytic membrane with hierarchical architecture: Photocatalytic and anti-bacterial activities, Water Res. 59 (2014) 207–218.

[33] N. Ma, X. Fan, X. Quan, Y. Zhang, Ag–TiO_2/HAP/Al_2O_3 bioceramic composite membrane: Fabrication, characterization and bactericidal activity, J. Memb. Sci. 336 (2009) 109–117.

[34] T. Tsuru, Inorganic Porous Membranes for Liquid Phase Separation, Sep. Purif. Rev. 30 (2001) 191–220.

[35] M. Clara, B. Strenn, N. Kreuzinger, Carbamazepine as a possible anthropogenic marker in

the aquatic environment: Investigations on the behaviour of carbamazepine in wastewater treatment and during groundwater infiltration., Water Res. 38 (2004) 947–954.

[36] T.A. Ternes, M. Meisenheimer, D. McDowell, F. Sacher, H.-J. Brauch, B. Haist-Gulde, G. Preuss, U. Wilme, N. Zulei-Seibert, Removal of pharmaceuticals during drinking water treatment, Environ. Sci. Technol. 36 (2002) 3855–3863.

[37] D. Avisar, I. Horovitz, L. Lozzi, F. Ruggieri, M. Baker, M.-L. Abel, H. Mamane, Impact of water quality on removal of carbamazepine in natural waters by N-doped TiO_2 photo-catalytic thin film surfaces, J. Hazard. Mater. 244-245 (2013) 463–471.

[38] H. Mamane, I. Horovitz, L. Lozzi, D. Di Camillo, D. Avisar, The role of physical and operational parameters in photocatalysis by N-doped TiO_2 sol–gel thin films, Chem. Eng. J. 257 (2014) 159–169.

[39] R. Grilli, D. Di Camillo, L. Lozzi, I. Horovitz, H. Mamane, D. Avisar, M. Baker, Surface characterisation and photocatalytic performance of N-doped TiO_2 thin films deposited onto 200 nm pore size alumina membranes by sol-gel methods, Mater. Chem. Phys. 159 (2015) 25–37.

[40] M.A. Baker, H. Fakhouri, R. Grilli, J. Pulpytel, W. Smith, F. Arefi-Khonsari, Effect of total gas pressure and O_2/N_2 flow rate on the nanostructure of N-doped TiO_2 thin films deposited by reactive sputtering, Thin Solid Films. 552 (2014) 10–17.

[41] C. Di Valentin, G. Pacchioni, A. Selloni, S. Livraghi, V.R. Cozzi, Characterization of Paramagnetic Species in N-doped TiO_2 Powders by EPR Spectroscopy and DFT Calculations, (2005) 11414–11419.

[42] R. Asahi, T. Morikawa, Nitrogen complex species and its chemical nature in TiO_2 for visible-light sensitized photocatalysis, Chem. Phys. 339 (2007) 57–63.

[43] H. Choi, a. C. Sofranko, D.D. Dionysiou, Nanocrystalline TiO_2 Photocatalytic Membranes with a Hierarchical Mesoporous Multilayer Structure: Synthesis, Characterization, and Multifunction, Adv. Funct. Mater. 16 (2006) 1067–1074.

[44] T. Tsuru, T. Kan-no, T. Yoshioka, M. Asaeda, A photocatalytic membrane reactor for gas-phase reactions using porous titanium oxide membranes, Catal. Today. 82 (2003) 41–48.

[45] U. Stafford, K.A. Gray, P. V Kamat, Photocatalytic degradation of 4-chlorophenol : The effects of varying TiO_2 concentration and light wavelength, J. Catal. 167 (1997) 25–32.

[46] Y. Wang, C. Feng, M. Zhang, J. Yang, Z. Zhang, Visible light active N-doped TiO_2 prepared from different precursors: Origin of the visible light absorption and photoactivity, Appl. Catal. B Environ. 104 (2011) 268–274.

[47] T. Ihara, M. Miyoshi, Y. Iriyama, O. Matsumoto, S. Sugihara, Visible-light-active titanium oxide photocatalyst realized by an oxygen-deficient structure and by nitrogen doping, Appl. Catal. B Environ. 42 (2003) 403–409.

[48] M.A. Mohamed, W.N.W. Salleh, J. Jaafar, A.F. Ismail, N.A.M. Nor, Photodegradation of phenol by N-Doped TiO_2 anatase/rutile nanorods assembled microsphere under UV and visible light irradiation, Mater. Chem. Phys. 162 (2015) 1–11.

[49] S. Larumbe, M. Monge, C. Gómez-Polo, Comparative study of (N, Fe) doped TiO_2 photocatalysts, Appl. Surf. Sci. 327 (2015) 490–497.

[50] K. Mehrotra, G.S. Yablonsky, A.K. Ray, Macro kinetic studies for photocatalytic degradation of benzoic acid in immobilized systems, Chemosphere. 60 (2005) 1427–1436.

[51] H.F. Lin, R. Ravikrishna, K.T. Valsaraj, Reusable adsorbents for dilute solution separation. 6. Batch and continuous reactors for the adsorption and degradation of 1,2-dichlorobenzene from dilute wastewater streams using titania as a photocatalyst, Sep. Purif. Technol. 28 (2002) 87–102.

[52] A.A. Assadi, A. Bouzaza, D. Wolbert, Photocatalytic oxidation of trimethylamine and isovaleraldehyde in an annular reactor: Influence of the mass transfer and the relative humidity, J. Photochem. Photobiol. A Chem. 236 (2012) 61–69.

[53] H. Lin, K.T. Valsaraj, Development of an optical fiber monolith reactor for photocatalytic wastewater treatment, J. Appl. Electrochem. 35 (2005) 699–708.

[54] J.-M. Herrmann, Heterogeneous photocatalysis: State of the art and present applications, Top. Catal. 34 (2005) 49–65.

[55] S. Malato, P. Fernández-Ibáñez, M.I. Maldonado, J. Blanco, W. Gernjak, Decontamination and disinfection of water by solar photocatalysis: Recent overview and trends, Catal. Today. 147 (2009) 1–59.

[56] S. Mozia, M. Tomaszewska, A.W. Morawski, Photocatalytic degradation of azo-dye Acid Red 18, Desalination. 185 (2005) 449–456.

[57] D. Chen, A.K. Ray, Photodegradation kinetics of 4-nitrophenol in TiO_2 suspension, Water Res. 32 (1998) 3223–3234.

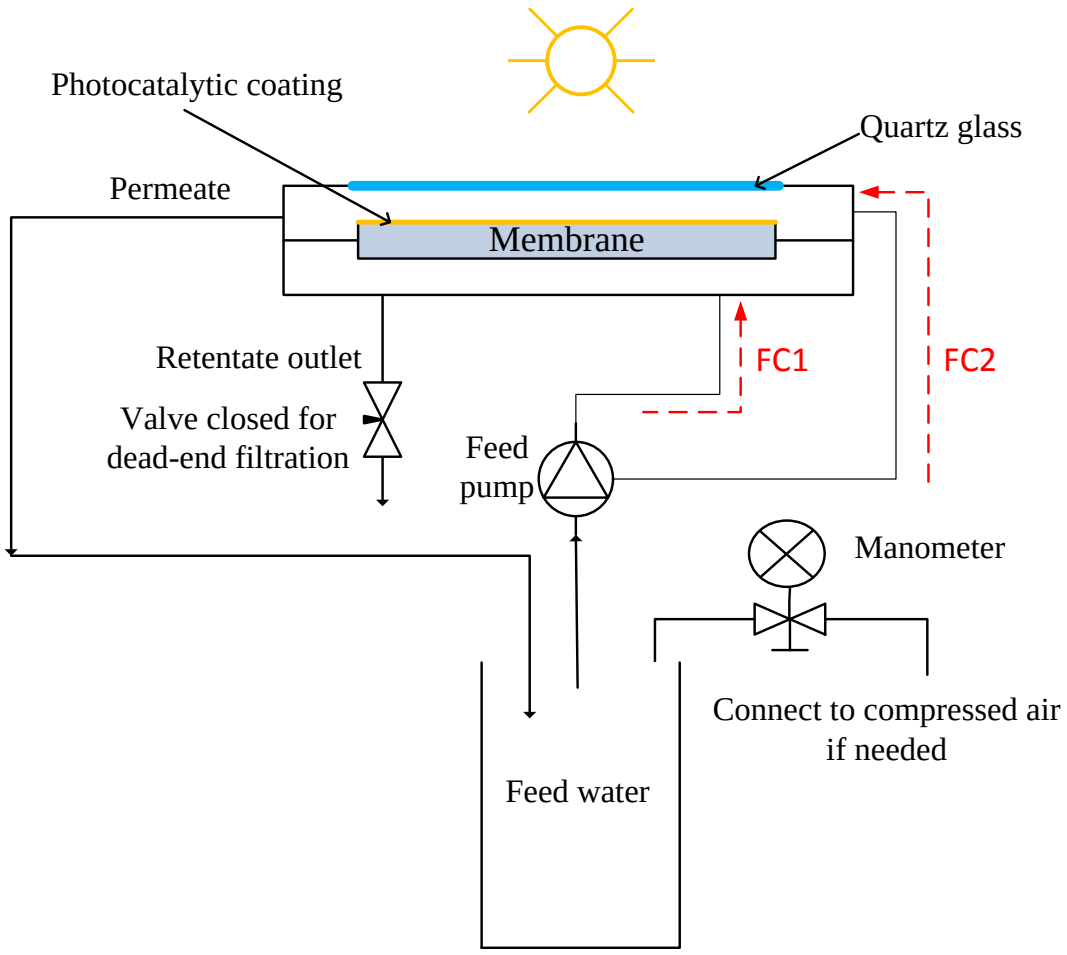

Fig. 1. Schematic diagram of a laboratory PMR system and flow configurations (FC1 – flow through the membrane and FC2 – flow without membrane permeation) used for ~~concurrent filtration and~~ solar photocatalytic degradation via recirculating ~~semi-~~batch operation mode.

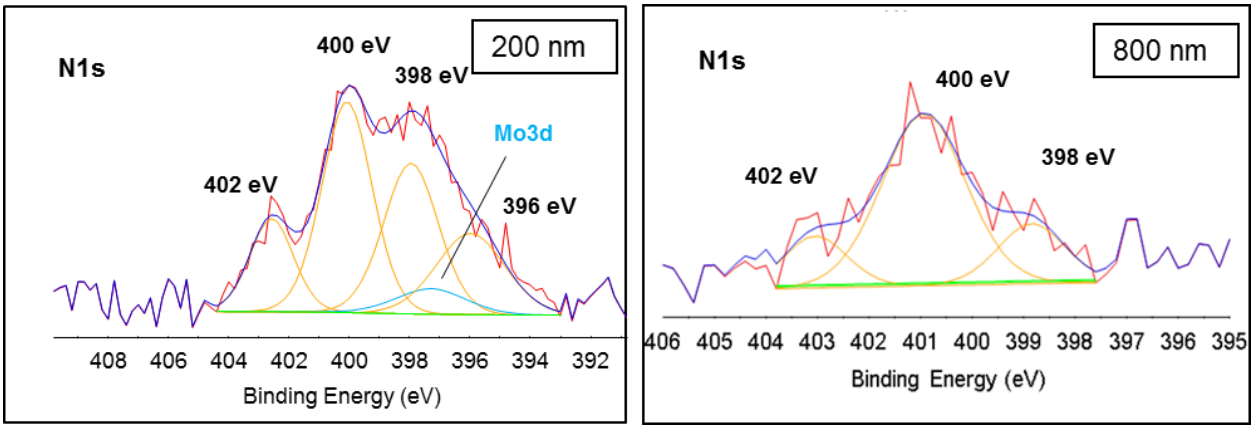

Fig. 2. High resolution N1s XPS spectra from the N-doped TiO_2 coated 200 nm and 800 nm pore size membranes

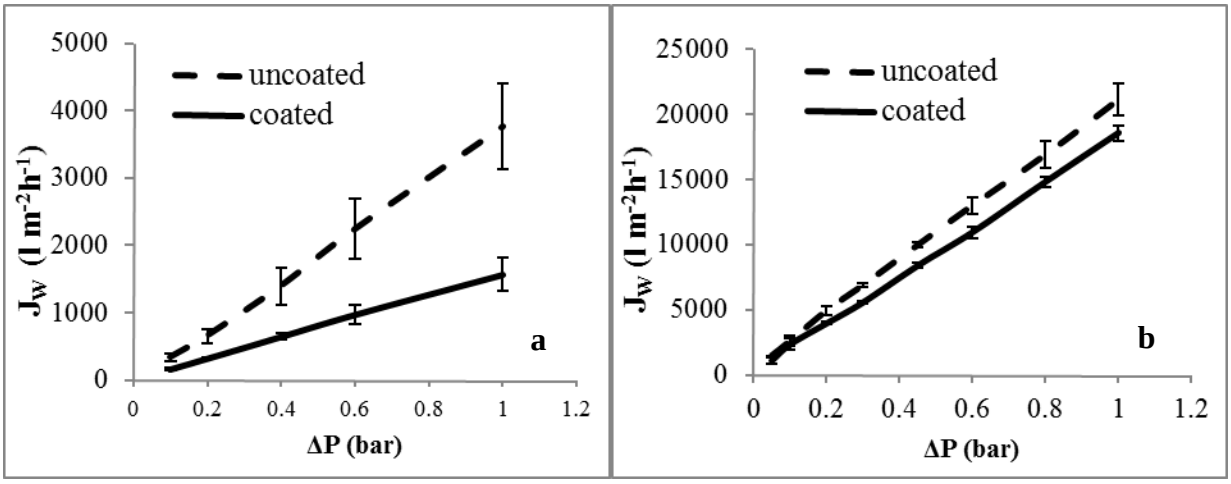

Fig. 3. Clean water flux as a function of pressure for a) Al_2O_3 200 nm and b) Al_2O_3 800 nm membranes

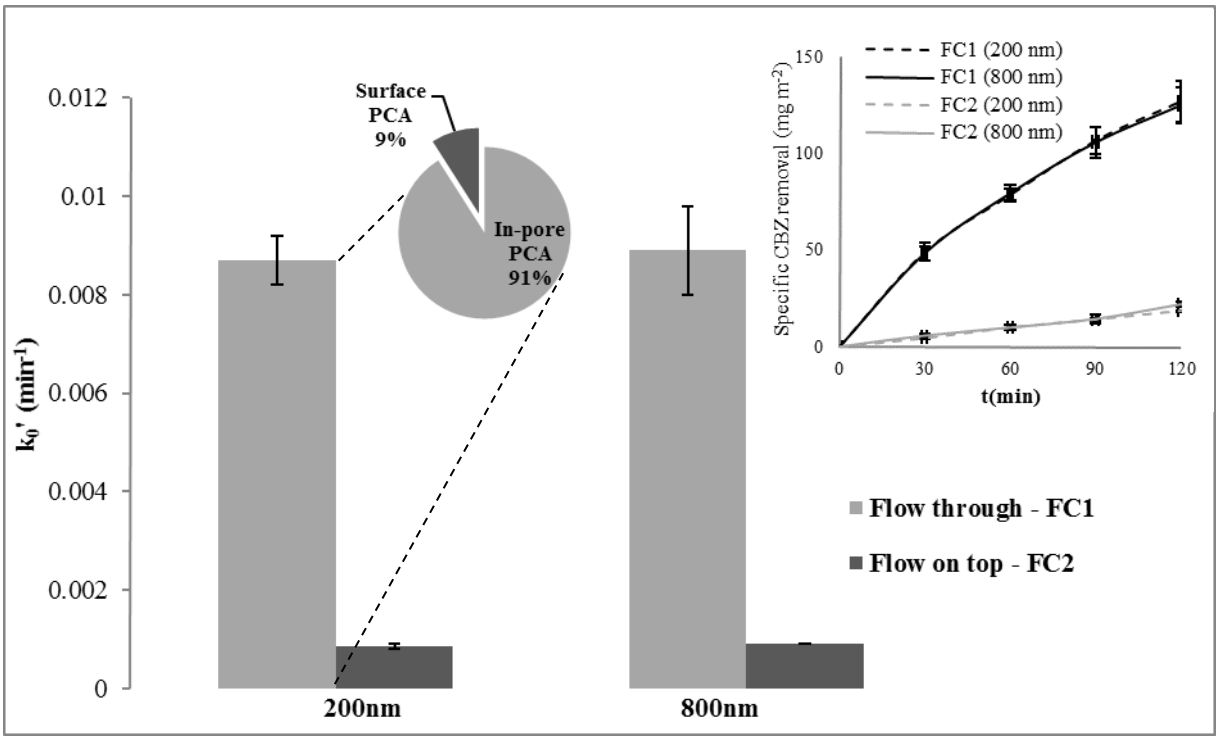

Fig. 4. CBZ degradation rate constant for two operation modes (Q=0.5 l h^{-1}): bulk flow through and surface flow over N-doped TiO_2 coated membranes: Al_2O_3 (200 nm) and Al_2O_3 (800 nm) (The insets depicts: on the left, the surface versus in-pore PCA components and on the right, the specific CBZ removal of FC1 and FC2).

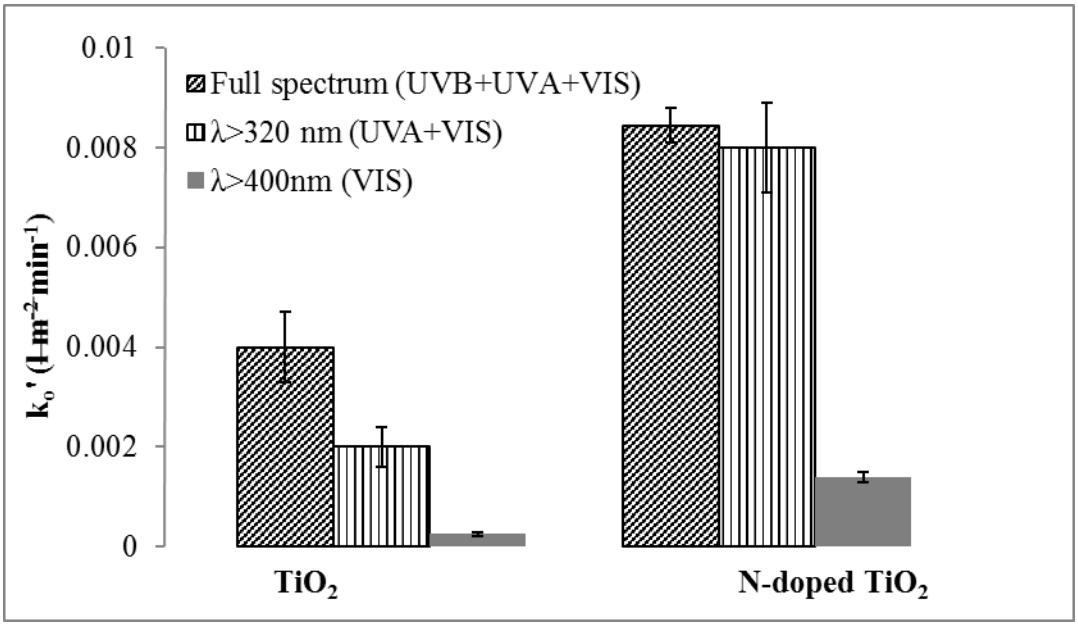

Fig. 5. CBZ removal by N-doped TiO_2 and TiO_2 coated membranes when exposed to the full spectrum (UVB+UVA+ *vis*), using a 320LP filter (UVA+ *vis*) and using a 400LP filter (*vis*)

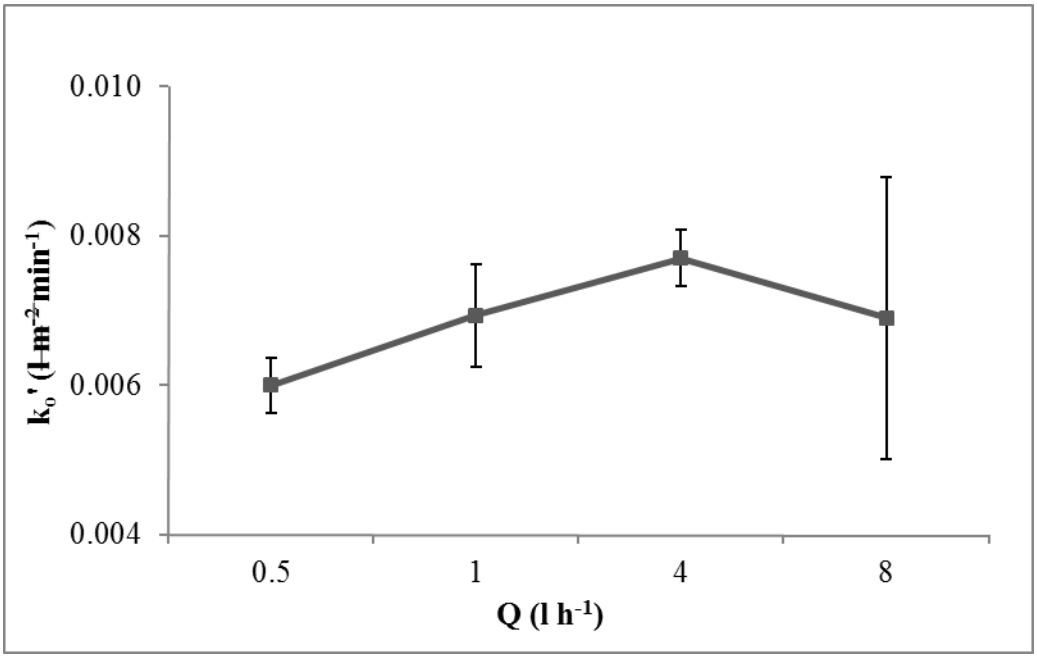

Fig. 6. The CBZ degradation rate constant as a function of flow rate

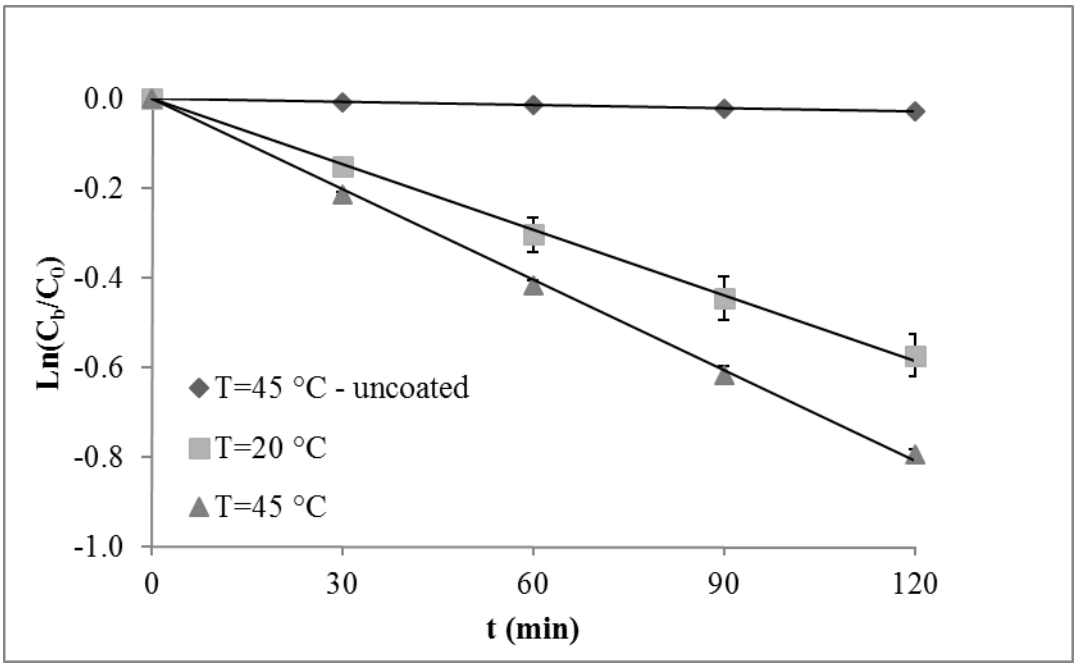

Fig. 7. CBZ degradation as a function of time at two feed solutions temperatures, T=20°C and T=45°C

Table 1: XPS-determined surface composition of the N-doped TiO_2-coated 200-nm and 800-nm pore size membranes.

Element	**C**	**O**	**Ti**	**Al**	**N**	**Si**	**Zr**	**Mo**	**Cu**	**Ca**	**Mg**	**F**
Concentration (at.%) 200 nm	12.6	62.7	18.2	5.1	0.9	-	0.4	0.2	-	-	-	-
Concentration (at.%) 800 nm	8.8	63.2	15.5	7.2	0.3	3.0	-	-	0.2	0.2	1.1	0.5

Table 2: Summary of percent contribution to CBZ degradation by UVB, UVA and visible (*vis*) ranges of the solar spectrum.

Coating type	**TiO_2**			**N-doped TiO_2**		
Spectrum range	**UVB**	**UVA**	***vis***	**UVB**	**UVA**	***vis***
% contribution out of total activity (i.e., full spectrum)	50	44	6	5	78	17